Published in final edited form as:

Nanoscale. 2016 April 28; 8(17): 9328–9336. doi:10.1039/c6nr01007e.

Cargo–shell and cargo–cargo couplings govern the mechanics of artificially loaded virus-derived cages†

Aida Llauró[a], **Daniel Luque**[b,c], **Ethan Edwards**[d], **Benes L. Trus**[e], **John Avera**[d], **David Reguera**[f], **Trevor Douglas**[d], **Pedro J. de Pablo**[a,g], and **José R. Castón**[b]

Pedro J. de Pablo: p.j.depablo@uam.es; José R. Castón: jrcaston@cnb.csic.es

[a]Department of Physics of the Condensed Matter, Universidad Autónoma de Madrid, 28049 Madrid, Spain

[b]Department of Structure of Macromolecules, Centro Nacional de Biotecnología (CNB–CSIC), Darwin 3, 28049 Madrid, Spain

[c]Centro Nacional de Microbiología/Instituto de Salud Carlos III, 28220 Majadahonda, Madrid, Spain

[d]Department of Chemistry, Indiana University, Bloomington, IN 47405, USA

[e]Imaging Sciences Laboratory, Center for Information Technology/National Institutes of Health, Bethesda, MD 20892-5624, USA

[f]Departament de Física Fonamental, Facultat de Física, Universitat de Barcelona, Martí i Franquès 1, 08028 Barcelona, Spain

[g]Solid Condensed Matter Institute IFIMAC, Universidad Autónoma de Madrid, 28049 Madrid, Spain

Abstract

Nucleic acids are the natural cargo of viruses and key determinants that affect viral shell stability. In some cases the genome structurally reinforces the shell, whereas in others genome packaging causes internal pressure that can induce destabilization. Although it is possible to pack heterologous cargoes inside virus-derived shells, little is known about the physical determinants of these artificial nanocontainers' stability. Atomic force and three-dimensional cryo-electron microscopy provided mechanical and structural information about the physical mechanisms of viral cage stabilization beyond the mere presence/absence of cargos. We analyzed the effects of cargo–shell and cargo–cargo interactions on shell stability after encapsulating two types of proteinaceous payloads. While bound cargo to the inner capsid surface mechanically reinforced the capsid in a structural manner, unbound cargo diffusing freely within the shell cavity pressurized the cages up to ~30 atm due to steric effects. Strong cargo–cargo coupling reduces the resilience of these nanocompartments in ~20% when bound to the shell. Understanding the stability of artificially loaded nanocages will help to design more robust and durable molecular nanocontainers.

†Electronic supplementary information (ESI) available: 6 figures, 3 tables and theory. See DOI: 10.1039/c6nr01007e

Correspondence to: Pedro J. de Pablo, p.j.depablo@uam.es; José R. Castón, jrcaston@cnb.csic.es.

Introduction

Synthetic biomimetic nanostructures are revolutionizing materials designed at the nanoscale. Inspired by nature, where intracellular structures act as optimized nanocompartments, new self-assembling biological systems have been generated with growing interest in biology, chemistry, and materials science.[1–7] Virus-like particles (VLP) showing a controlled hierarchical assembly are easy to produce, and their structure can accommodate modifications of their inner and/or outer surfaces. These attributes enable the incorporation of artificial cargos in the VLP, such as small molecules,[7–9] metal nanoparticles[10–12] or proteins,[8] to produce hybrid materials that can be used for a broad range of applications. The confinement of proteins inside VLP permits the modulation, spatial control and protection of their enzymatic activity in a variety of environments, and has evident interest for pharmaceutical and nano-technological applications.[13–15]

The development of robust, stable nanocages able to maintain their structure is crucial for their durability under harsh environmental conditions, and some successful strategies can be adopted from nature. Genetic material can reinforce natural viral shells after packing *via* structural interaction with the viral shell, similar to the way beams buttress the structure of a building.[16,17] In other cases, the genome destabilizes the viral shell by inducing outward pressurization that stiffens the viral particles.[18–20] Therefore, the stability of protein-derived cages loaded with heterologous proteins depends not only on the presence of its internal cargo, but also on the mutual cargo–shell and cargo–cargo interplay, as in the case of their natural counterparts.

Virus-like particles (VLP) derived from the *Salmonella typhimurium* bacteriophage P22 are suitable models to address some of these questions, as it is a versatile and well-characterized system in virology and nanomaterial synthesis.[21,22] The P22 VLP capsid is built of 420 copies of a coat protein (CP) that assembles into a $T = 7$ icosahedral shell with the aid of 100–300 copies of scaffolding proteins (SP); the SP C-terminal helix–loop–helix motif interacts with the CP. In contrast to authentic phages, these VLPs have 12 identical pentons with no portal.[23] P22 VLP procapsids (PC) undergo a series of well-defined structural transitions after heating that generate mature viral shells (EX particles), emulating bacteriophage P22 maturation.[21,22,24] This capsid transition (PC $\rightarrow$ EX) involves an increase in the internal volume of ~35%, as well as capsid shell thinning and a decrease in its porosity.

Heterologous expression of CP and N-terminal-truncated SP fused to other gene products results in self-assembly of the PC (59.6 nm outer diameter, 46 450 nm^3 internal volume); heating at 65 °C for 20 min yields the EX (64.8 nm, 71 900 nm^3) (Fig. 1A). We used the SP fusion strategy to incorporate enhanced green fluorescence protein (EGFP) or β-glucosidase from the hyperthermophile *Pyrococcus furiosus* (CelB) into the VLP interior when expressed in *Escherichia coli* together with CP (Fig. 1B). As the interaction between EGFP monomers is anticipated to be weaker than those between CelB monomers, which form spontaneous tetramers inside the shell,[25] we used these two proteins to study the effects of cargo–cargo coupling. The ability of the PC structure to mature into the EX morphology while maintaining its cargo allowed us to address the effects of cargo–shell coupling. During

maturation, the SP C-terminal segment of the SP-cargo protein is unbound from the interior surface shell, resulting in soluble cargo molecules inside the EX.[21,24,26–32]

Here we combined the mechanical and structural information obtained from atomic force microscopy (AFM) and three-dimensional cryo-electron microscopy (3D cryo-EM) to describe physico-chemical mechanisms that influence the stability of synthetic P22 protein cages. Our results show that the interplay between the cargo and the shell determines whether the mechanical reinforcement is structure- or pressure-induced, as happens in natural viral cages. Cargo bound to the shell provides structural reinforcement to the P22 procapsid, although a strong cargo–cargo interaction renders particles more brittle. In the expanded form, cargo–shell interactions are removed and the SP-associated cargo proteins remain inside the particle in a "free" soluble state that pressurizes the expanded structure up to 3 MPa.

Results and discussion

Three-dimensional structure of cargo-loaded P22 VLP

We used 3D cryo-EM to analyze the structures of two morphologies of heterologous bacteriophage P22 $T = 7$ VLP, termed PC and EX, loaded with a cargo of EGFP or CelB. Empty PC and EX were included as controls (Fig. 2). We used HPLC size exclusion chromatography with multi-angle light scattering (MALS) to determine the number of cargo copies per particle, and found 128 ± 1 CelB and 220 ± 5 EGFP monomers. Fig. 2A shows cryo-EM images of these purified P22 VLP with different morphologies, imaged at −170 °C using a 200 kV cryo-electron microscope. A 3D reconstruction (3DR) was calculated for each of the six sets of particle types (Fig. 2B–D). Based on a Fourier shell correlation (FSC) coefficient, the resolutions achieved were between 12 and 16 Å (Fig. S1[†]). Particle diameters were determined from radial density profiles from the 3DR (Fig. 2E). Whereas spherical PC (empty, EGFP- or CelB-loaded) had a 298 Å outer radius, EX form measured 324 Å. This capsid expansion range is similar in bacteriophages P22, λ and HK97.[33]

Cargo-loaded PC and EX had the same size and general morphology as empty PC and EX. The P22 PC were $T = 7$ isometric structures formed by 72 capsomers, 60 of which are skewed CP hexamers and 12 are CP pentamers, as they lack the portal structure (Fig. 2B, top).[22] Empty PC showed densities at the inner surfaces of the hexamers, due to SP C-terminal residues, which cannot be accounted for by the CP (Fig. 2C, arrows), as reported.[21,22,24]

Images of EGFP- or CelB-loaded PC (EGFP-PC or CelB-PC) were darker than the empty counterparts (Fig. 2A), which indicated the presence of packed cargos. After imposing icosahedral symmetry, the 3DR showed that cargo density (within a 220 Å radius) was organized as a thick shell beneath the PC shell, with numerous connections to the PC inner surface (Fig. 2C, middle [EGFP-] and right [CelB-PC]). As in *in vivo*-matured virions, P22 EX were more angular than PC, and the hexons became symmetrical hexamers (Fig. 2D). Heat-induced capsid maturation untethered EGFP- or CelB-fused SP from the EX interior

[†]Electronic supplementary information (ESI) available: 6 figures, 3 tables and theory. See DOI: 10.1039/c6nr01007e

surface and cargos were observed as free densities in the capsid interior (Fig. 2A), in concordance with wild-type P22 procapsid release of SP after heating.[34]

AFM topographical analysis of empty and cargo-loaded P22 VLP *in vitro*

Fixation of protein shells to a flat substrate *via* hydrophobic[35] and/or electrostatic interactions[36] is a requisite for AFM. Each protein shell has individual features such as hydrophobic patches or local charge densities, resulting in distinct attachment forces. For a specific shell, these forces can even reduce the height of the softest virus-like morphologies[37] although this is not always the case.[20,38]

The precise combination of factors that leads to this partial collapse remains undefined, but so far a decrease in height has been always accompanied by a decrease in the mechanical stiffness of the specimen.

Representative AFM images of each VLP type adsorbed on glass (see Materials & methods) showed partial collapse (Fig. 3A), which allowed us to carry out a comparative study of particle deformability. Whereas empty VLP showed a height decrease of ~10% compared with their native size in cryo-EM, cargo-loaded VLP maintained heights near 100% of the cryo-EM value (Fig. 3B). The limited shell deformation of cargo-loaded VLP suggested that these particles were more rigid than their empty counterparts.

Cargo–cargo and cargo–shell interactions determine P22 PC mechanics

VLP mechanical stability can be assessed systematically using nano-indentation curves of individual particles. This procedure involves deformation of single particles with an AFM tip until the specimen breaks. The force *vs.* the indention curve (FIC) obtained in these experiments provides two mechanical parameters that are linked to the rigidity and brittleness of the particle probed.[39,40] Fig. 4A shows a characteristic FIC performed on an intact EGFP-PC. AFM images taken before and after the FIC demonstrated the rupture of the shell, which in this case caused a crack associated with a reduction in height from 57 to 47 nm (Fig. 4A, right). Other examples of this sort of experiments can be found in Fig. S2.†

Particle rigidity is related to the slope of the curve (also termed spring constant, k) and the maximum deformation the particle can withstand before rupturing defines the critical indentation (δ_{critical}), a measure of brittleness.[41] The ratio between this critical deformation and particle height (h) before deformation accounts for critical strain, $\varepsilon_{\text{critical}}=\frac{\delta_{\text{critical}}}{h}$ (Fig. 4A, inset), which is the parameter that we used in our experiment to establish differences in particle brittleness.[41] Our AFM data showed that EGFP- and CelB-PC were more rigid than empty PC (Fig. 4B top, Table S1†), in agreement with our initial topographical analysis (Fig. 3). To determine the cause of this difference in stiffness we analyzed the cryo-EM maps in detail. Comparison of the average radial densities of empty and full PC particles indicated that most cargo localized in a shell beneath the capsid wall within a 216–107 Å radius (Fig. 2E, top). Whereas the empty PC structure showed a single spherical layer corresponding to the capsid shell, full PC presented an extra concentric layer corresponding to cargos. These data suggested that the stiffening was caused by a structural reinforcement that could be evaluated by continuous elasticity modeling. Simplification of these complex structures to

homogeneous shells[42–45] permits estimation of the ratio of the Young's modulus of the capsid (E_s) and the cargo (E_c). The radial density derived from the cryo-EM data indicated that empty- and loaded-PC had effective thicknesses of ~7.5 and ~17.5 nm, respectively (Fig. 2E). Finite element modeling estimated E_s/E_c of 7 and 10 for EGFP and CelB cargos, respectively (ESI, Fig. S3A†), indicating that the capsid shell is approximately ten times more rigid than the cargo "shell". Therefore, the container might be able to offer protection to the contents because of its higher Young's modulus.

Whereas both packed cargos have a similar influence on the rigidity of the particles, there was a difference in brittleness between EGFP- and CelB-loaded PC compared to empty shells (Fig. 4B bottom, Table S1†). To evaluate this difference in strain, we performed docking analysis of the P22 CP model [Ca model, Protein Data Bank (PDB) ID 2XYY,[21] and the SP C-terminal region (residues 238–303, PDB ID 2GP8)[46]] in the empty and loaded PC cryo-EM density maps. The SP C terminus fitted well in the triangular density at the internal surface of the PC skewed hexamers (Fig. 4C left, blue). This SP-related density was also well preserved in the EGFP-PC at the same radial position, and showed the connections between the CP shell and cargo (Fig. 4C middle, green). CelB-PC connections were more disordered in this region than empty and EGFP-PC, and SP-mediated connections were irregular and less defined (Fig. 4C right, red). This scenario is compatible with the existence of fewer SP-mediated connections for CelB-PC than for EGFP-PC. Whereas EGFP molecules remain as monomers, CelB monomers strongly interact to form tetramers[25] whose assembly could affect the SP–CP interaction. CelB monomers are connected to CP by a 123 amino acid linker that joins the cargo with the SP–CP binding domain. We propose that CelB tetramers inside the PC shell would tighten some of these SP-mediated connections, leading to an additional geometrical constraint that might reduce capsid subunit mobility during nanoindentations (Fig. 4D, top). In contrast, the monomeric conditions of EGFP would not impose any constraint on the SP linkers (Fig. 4D, bottom). The reduced mobility of the CelB-PC structural subunits would render more brittle particles, resulting in lower critical strain for CelB-PC ($\varepsilon_{critical}$ = 0.14) than for EGFP-PC ($\varepsilon_{critical}$ = 0.17) (Table S1†).

Beyond the breaking force, indentation curves (Fig. S2,† top) undergo an abrupt decay informing about how fast the tip penetrates the virus. Although with high variability, post-fracture curves show that the cantilever decays to low deflection values quicker on empty PC than on filled PC, thus revealing that there are less obstacles impairing the tip indentation inside the fractured empty PC. We tentatively hypothesize that the cargo, well bound to the PC capsid, prevents the tip from indenting inside the virus.

Mechanics of empty and cargo-loaded EX structures

During the transition from PC to EX, the SP domains release the CP and escape from the capsid, resulting in empty EX particles.[24] However, in the case of loaded particles the SP fused to EGFP or CelB structures cannot escape and become free inside the EX after detaching from the capsid wall. We analyzed the mechanics of three expanded protein cages (empty, CelB- and EGFP-EX) to establish differences between them. Fig. 5A shows a representative nanoindentation curve performed on a CelB-EX, with the AFM images before

(Fig. 5A, top right) and after the tip-induced breakage (Fig. 5A, bottom right). Statistical analysis of the mechanical properties of the three EX types showed that whereas cargo increased rigidity, $\varepsilon_{critical}$ did not vary (Fig. 5B). Compared with the AFM data for CelB-PC, the lack of influence of this cargo on EX brittleness is likely related to the detachment of SP domains that connected CelB tetramers to the shell, which no longer represent a geometrical constraint. EGFP monomers and CelB tetramers remained unanchored, free to diffuse within the EX cage (Fig. 5C). This might justify why the full EX particles do not differentiate from the empty ones in the post-fracture nanoindentation patterns: both particles reach low deflection values as soon as they are broken (Fig. S4†). In contrast with PC structures, the cargo is unbound from the capsid shell. We hypothesize that proteins can diffuse out as soon as the capsid is cracked and they do not impair the tip indentation in the fractured shell. In addition, the mechanical properties (*i.e.*, breaking force and rigidity) of EX increased significantly in comparison with PC, as a consequence of the stabilization gained by the VLPs during capsid maturation (Table S1, Fig. S2 and S4†).[22]

Because no permanent structural contacts exist between the cargo and the capsid shell in EX capsids, the increased rigidity in EX (Fig. 5B, top) could be due to an osmotic pressure arising from the different concentration between the inner shell and the surroundings. This difference would drive water molecules into the shell and increase the pressure of the cages. Alternatively, it might be caused by electrostatic repulsion between cargo molecules retained within the capsid. To determine which of these mechanisms was responsible for the capsid reinforcement, we modeled our system and performed new AFM experiments.

Pressurization of EX VLP

Regardless of its physical origin, we can estimate the magnitude of the internal pressure in loaded EX using the continuous elastic prediction for rigidity of a pressurized thin spherical shell indented by a point force.[47]

$$k_1 = \frac{\pi}{2} k_0 \frac{(\tau^2 - 1)^{\frac{1}{2}}}{\operatorname{arctanh}\left[(1 - \tau^{-2})^{\frac{1}{2}}\right]} \quad (1)$$

Here, $\tau = pR_1/k_0$ is a dimensionless parameter that compares the relative relevance of pressure p against the elastic constant of the unpressurized shell, k_0, and R_1 the internal radius of P22 EX, considered effectively as a sphere (R_1 = 29.1 Taking $k_0 = k_{EX}$ = 0.21 N m^{-1}, $k_1 = k_{EGFP\text{-}EX} = k_{CelB\text{-}EX}$ = 0.27 N m^{-1}, and solving eqn (1) for p, an estimate of 3 ± 1 MPa is obtained for the increase in internal pressure after cargo internalization, a value that was corroborated by Finite Element Simulations (Fig. S3B†).

The osmotic pressure generated from a freely moving cargo constrained to the EX interior depends on the nature of the interactions between the cargo molecules and between the cargo and the inner capsid wall. The simplest influence stems from steric interactions between cargo molecules and the fact that they cannot escape from the capsid. The irregular geometry of the cargo, enhanced by the presence of the SP linker and the helix–loop–helix motif attached to it, makes accurate quantification difficult. Its magnitude can nonetheless be estimated by modeling the cargo molecules as uncharged hard spherical colloids with an

effective radius R_{HS}. In this approach, the expression for this "hard spheres" contribution to the osmotic pressure is[48,49]

$$p_{HS}=k_B T\rho\frac{(1+\eta+\eta^2+\eta^3)}{(1-\eta^3)} \quad (2)$$

where $k_B = 1.38 \times 10^{-23}$ m^2 kg K s^{-2} is the Boltzmann constant, $T = 300$ K is the temperature, ρ is the number density of the cargo inside the particle, and $\eta=\frac{V_{CARGO}}{V_{EX}}=\frac{N \times 4/3\pi {R_{HS}}^3}{V_{EX}}$ is the packing fraction, defined as the volume occupied by the cargo divided by the available volume in the capsid (Tables 1 and S2†). This assumption allowed us to evaluate the effective hard sphere radius (R_{HS}) needed to obtain the pressure values estimated in the experiments (eqn (1)).

Size exclusion chromatography coupled to multi-angle light scattering (SEC-MALS) indicated that, on average, the mass of loaded particles decreased slightly after expansion, as reported in previous studies.[3] In our bulk experiments, loaded EX lost 20 CelB (16%) and 64 EGFP (30%) monomers in comparison with their PC forms. This loss of material was probably related to defective particles. Shell defects, such as missing pentamers, allow cargo molecules to leave the cavity, and thus only the particles flawed or broken during thermal expansion would be responsible for this loss of average mass measured by SEC-MALS. AFM permits topographic characterization of each EX particle and resolves capsomeric defects, thus allowing the selection of intact particles that have presumably not lost any cargo molecules. Therefore, we assumed that in our AFM experiments PC and EX capsids contained the same amount of monomers, and we used the PC values to calculate the different packing factors and the effective radii.

In the case of CelB-EX, in which $N = 128 \pm 1$ monomers were encapsulated per capsid and the estimated pressure was $p = 3 \pm 1$ MPa, the effective radius was R_{HS}(CelB) = 7.8 nm. For EGFP-EX, with $N = 220 \pm 5$ monomers encapsulated and the same pressure as CelB-EX, the effective radius was R_{HS}(EGFP) = 3.9 nm. These radii result in volumes slightly larger than CelB tetramers (10.1 × 10.1 × 5.7 nm^3)[50] and EGFP monomers (4.8 × 3.3 × 3.5 nm^3)[51] (Table S2†). The slight overestimation of the hard-sphere radii over the characteristic dimensions of the cargo units is probably due to the presence of the SP and the linker attached to the cargo proteins, leading to effective excluded volumes that are larger than the actual volumes occupied by the bare cargo molecules.

A second contribution to the pressure could arise from the electrostatic repulsion between the cargo molecules or/and the cargo and the shell. The magnitude of this influence could be estimated in two ways, by considering a solution of N effective charged spheres in an electrolyte[52] or through the concept of Donnan equilibrium.[53] Both calculations led to theoretical pressure values that were negligible compared with the values obtained in our experiments (ESI†). The electrostatic contribution of natural cargos such as dsDNA has been detected in natural viral cages by altering the ionic strength or using a condensing agent such as spermidine to screen DNA–DNA repulsion, which reduces virus rigidity.[19,20,54] To assess

the relevance of the electrostatic effects experimentally, we carried out AFM nanoindentations on loaded EX at low ionic strength and in the presence of spermidine (Fig. S5†). In both cases, particle stiffness did not change, which supported the hypothesis used in theory that the electric nature of the cargo made no significant contribution (ESI†).

Conclusions

Our data indicate that the presence of a cargo stiffens the cages in two different ways. In the case of PC, when the cargo is linked to the shell through the C-terminal SP motif, the capsid is reinforced structurally. For EX capsids, however, cargo–shell interactions are lost and the increase in rigidity is due to the different concentration of osmolyte (CelB tetramers or EGFP monomers) between the inside of the capsid shell and the surroundings. This different concentration drives water molecules inside the particle creating an osmotic pressure of ~30 atm, a value comparable to the DNA-induced pressurization in natural viruses (40–60 atm for phi29,[19,55] 20 atm for lambda,[56] 10 atm for P22 phages,[57,58] and 30 atm for human adenovirus[20]). We also found that geometrical constrains imposed by the tetrameric structure of the CelB cargo makes PC brittle.

Overall, our results show the interplay between the cargo and the shell contributes to the reinforcement of the capsid *via* different physical mechanisms. Understanding these mechanisms and their molecular determinants would permit the optimization of their performance and robustness in harsh environments and it is fundamental for their development as protective shields against proteases, desiccation and/or thermal destabilization.

Materials and methods

Biochemical and genetic analyses

Proteins were cloned, expressed and purified, and analyzed by size exclusion chromatography with multi-angle light scattering and refractive index detection was performed as described.[3,4,7] Plasmids containing the genes for coat protein and cargo proteins of interest fused to scaffold protein (EGFP-SP[3], CelB-SP[25]) were transformed into BL21 (DE3) *Escherichia coli* (Novagen) for protein expression. The transformed *E. coli* cells were grown to an OD_{600} = 0.6, induced with isopropyl b-D-thiogalactopyranoside (IPTG), and grown for an additional 4 h before cells were collected by centrifugation at 4500 rpm. Cells were resuspended in PBS pH 7, lysed by sonication, centrifuged (at 12 000 rpm) to remove cell debris, and virus particles were isolated by ultracentrifugation through a sucrose cushion. The resuspended pellet was further purified on a Sephacryl (S-500; GE Healthcare) size exclusion column in PBS pH 7 (1 ml min^{-1}). For SEC-MALS analysis, samples were analyzed on a Dawn 8 instrument (Wyatt Technologies, Santa Barbara, CA). Samples were separated by Agilent 1200 HPLC on a WTC-0200S size exclusion column (Wyatt Technologies) and monitored with a UV-Vis detector (Agilent), a Wyatt HELEOS Multi Angle Laser Light Scattering (MALS) detector, a quasi-elastic light scattering detector (QELS), and an Optilab rEX differential refractometer (Wyatt Technologies). The Wyatt Astra 6 software determined the average molecular weight (M_w) and radius of gyration (R_g) values.

Cryo-EM and image processing

Samples (5 ml) were applied to Quantifoil R 2/2 holey grids, blotted, and plunged into liquid ethane. Cryo-EM images were recorded under low-dose conditions with a FEI Eagle CCD camera using a Tecnai G2 electron microscope equipped with a field emission gun operating at 200 kV and at a detector magnification of 69 444× (2.16 Å per pixel sampling rate).

General image processing operations were performed using Xmipp,[59] and graphics were produced using UCSF Chimera.[60] The Xmipp automatic picking routine was used to select particles. Defocus was determined with CTFfind[61] and CTF phase oscillations were corrected in the images by flipping them in the required lobes. Homogeneous populations were selected by two-dimensional classification using the Xmipp CL2D reference-free clustering routine.[62] Published structures of P22 PC and EX (PDB 2XYY and 2XYZ)[21] were filtered to 30 Å, size-scaled and used as initial models for their respective samples. The Xmipp iterative projection matching routine[63] was used to determine and refine the particle origin and orientation. For the CelB tetramer, an artificial noise model was used as starting reference for parallel iterative angular refinement using the EMAN program.[64] Once converged, the resulting model was selected and refined using the Xmipp iterative projection matching routine. For PC, EX and CelB, 90% of the particles were included in the final 3DR, and resolution was assessed by FSC between independent half dataset maps (Fig. S1[†]). The final map of the CelB tetramer included 11 432 particles, and resolution for the 0.5 and 0.3 criteria was 16.4 and 14.5 Å, respectively. The UCSF Chimera fitting routine was used to dock the crystallographic models of PC, EX, SP and Pyrococcus b-glucosidase CelB (PDB 2XYY, 2XYZ, 2GP8 and 3APG, respectively) in the cryo-EM maps. The 3D reconstructions are deposited in the Electron Microscopy Data Bank (http://www.ebi.ac.uk/pdbe/emdb) with accession no. EMD-3171 (empty PC), EMD-3172 (EGFP-PC), EMD-3173 (CelB-PC), EMD-3174 (empty EX), EMD-3175 (EGFP-EX), EMD-3176 (CelB-EX) and EMD-3177 (CelB tetramer).

AFM

AFM experiments were performed as described,[45] using a Nanotec Electrónica microscope (Madrid, Spain) operating in jumping mode plus.[65] Imaging forces were maintained below 150 pN. Rectangular silicon-nitride cantilevers (RC800PSA, Olympus, Center Valley, PA) with a nominal spring constant of 0.05 N m^{-1} were calibrated before each measurement by Sader's method.[66] Experiments were carried out under standard buffer conditions (100 mM phosphate, 50 mM NaCl, pH 7) at a controlled temperature of 17 °C. A 20 ml drop of diluted stock solution was incubated on previously silanized glass coverslips. Cleaning and functionalizing of glass surfaces was performed as described.[42] After 30 min, the sample was washed with buffer solution to a volume of 90 ml. AFM images were processed with WSxM software. AFM control experiments were performed under two conditions, at low ionic strength (50 mM phosphate, 25 mM NaCl, pH 7) and with 1 mM spermidine (100 mM phosphate, 50 mM NaCl, 1 mM spermidine, pH 7). Details of the procedure are found in the ESI.[†]

Nanoindentation was done at a loading rate of 60 nm s^{-1} with forward elongation of 100 nm. Force-*vs.*-indentation curves (FIC) were obtained from force-*vs.*-*Z*-piezo curves as

reported.[45] The elastic constant was obtained by fitting the initial linear part of each FIC. Breaking force and critical indentation were measured with WsxM_ENREF_65.[67] A summary of the number of particles and average values of the mechanical properties analyzed are detailed in the ESI.†

Supplementary Material

Refer to Web version on PubMed Central for supplementary material.

Acknowledgments

We thank C. Mark for editorial assistance. This work was supported by grants from the Spanish Ministry of Economy and Competitivity (FIS2011-22603 and FIS2011-16090-E to DR, FIS2014-59562-R to PJP, FIS2015-71108-REDT to DR, PJP and JRC and BFU2014-55475-R to JRC), the Comunidad Autónoma de Madrid (S2013/MIT-2807 to JRC), Fundación BBVA to PJP, NSF-BMAT DMR-1507282 to TD, and the Intramural Research Program of the NIH and the Center for Information Technology (to BLT).

Notes and references

1. Yeates TO, Kerfeld CA, Heinhorst S, Cannon GC, Shively JM. Nat Rev Microbiol. 2008; 6:681–691. [PubMed: 18679172]
2. Cheng S, Liu Y, Crowley CS, Yeates TO, Bobik TA. Bioessays. 2008; 30:1084–1095. [PubMed: 18937343]
3. O'Neil A, Reichhardt C, Johnson B, Prevelige PE, Douglas T. Angew Chem, Int Ed. 2011; 50:7425–7428.
4. Patterson DP, Prevelige PE, Douglas T. ACS Nano. 2012; 6:5000–5009. [PubMed: 22624576]
5. Tanaka S, Kerfeld CA, Sawaya MR, Cai F, Heinhorst S, Cannon GC, Yeates TO. Science. 2008; 319:1083–1086. [PubMed: 18292340]
6. Kerfeld CA, Sawaya MR, Tanaka S, Nguyen CV, Phillips M, Beeby M, Yeates TO. Science. 2005; 309:936–938. [PubMed: 16081736]
7. Lucon J, Qazi S, Uchida M, Bedwell GJ, LaFrance B, Prevelige PE Jr, Douglas T. Nat Chem. 2012; 4:781–788. [PubMed: 23000990]
8. Kang S, Uchida M, O'Neil A, Li R, Prevelige PE, Douglas T. Biomacromolecules. 2010; 11:2804–2809. [PubMed: 20839852]
9. Qazi S, Liepold LO, Abedin MJ, Johnson B, Prevelige P, Frank JA, Douglas T. Mol Pharmaceutics. 2012; 10:11–17.
10. Reichhardt C, Uchida M, O'Neil A, Li R, Prevelige PE, Douglas T. Chem Commun. 2011; 47:6326–6328.
11. Uchida M, Kosuge H, Terashima M, Willits DA, Liepold LO, Young MJ, McConnell MV, Douglas T. ACS Nano. 2011; 5:2493–2502. [PubMed: 21391720]
12. Uchida M, Kang S, Reichhardt C, Harlen K, Douglas T. Biochim Biophys Acta, Gen Subj. 2010; 1800:834–845.
13. Patterson DP, Rynda-Apple A, Harmsen AL, Harmsen AG, Douglas T. ACS Nano. 2013; 7:3036–3044. [PubMed: 23540530]
14. Schwarz B, Douglas T. Wiley Interdisciplinary Reviews: Nanomedicine and Nanobiotechnology. 2015
15. Manchester, M.; Steinmetz, NF. Viruses and nanotechnology. Springer; 2009.
16. Carrasco C, Carreira A, Schaap I, Serena P, Gomez-Herrero J, Mateu M, De Pablo P. Proc Natl Acad Sci U S A. 2006; 103:13706–13711. [PubMed: 16945903]
17. Carrasco C, Castellanos M, De Pablo PJ, Mateu MG. Proc Natl Acad Sci U S A. 2008; 105:4150–4155. [PubMed: 18334651]
18. Gelbart WM, Knobler CM. Science. 2009; 323:1682–1683. [PubMed: 19325104]

19. Hernando-Perez M, Miranda R, Aznar M, Carrascosa JL, Schaap IAT, Reguera D, De Pablo PJ. Small. 2012; 8:2366–2370. [PubMed: 22648860]
20. Ortega-Esteban A, Condezo GN, Pérez-Berná AJ, Chillón M, Flint SJ, Reguera D, San Martín C, De Pablo PJ. ACS Nano. 2015; 9(11):10826–10833. [PubMed: 26491879]
21. Chen DH, Baker ML, Hryc CF, DiMaio F, Jakana J, Wu W, Dougherty M, Haase-Pettingell C, Schmid MF, Jiang W, Baker D, King JA, Chiu W. Proc Natl Acad Sci U S A. 2011; 108:1355–1360. [PubMed: 21220301]
22. Parent KN, Khayat R, Tu LH, Suhanovsky MM, Cortines JR, Teschke CM, Johnson JE, Baker TS. Structure. 2010; 18:390–401. [PubMed: 20223221]
23. Bhardwaj A, Olia AS, Cingolani G. Curr Opin Struct Biol. 2014; 25:1–8. [PubMed: 24878339]
24. Prasad BVV, Prevelige PE, Marietta E, Chen RO, Thomas D, King J, Chiu W. J Mol Biol. 1993; 231:65–74. [PubMed: 8496966]
25. Patterson DP, Schwarz B, El-Boubbou K, van der Oost J, Prevelige PE, Douglas T. Soft Matter. 2012; 8:10158–10166.
26. Bazinet C, King J. Annu Rev Microbiol. 1985; 39:109–129. [PubMed: 2932996]
27. Kang S, Prevelige PE. J Mol Biol. 2005; 347:935–948. [PubMed: 15784254]
28. Jiang W, Li Z, Zhang Z, Baker ML, Prevelige PE, Chiu W. Nat Struct Mol Biol. 2003; 10:131–135.
29. Prevelige PE Jr, Thomas D, Aubrey KL, Towse SA, Thomas GJ Jr. Biochemistry. 1993; 32:537–543. [PubMed: 8422364]
30. Earnshaw WC, Casjens SR. Cell. 1980; 21:319–331. [PubMed: 6447542]
31. Botstein D, Waddell CH, King J. J Mol Biol. 1973; 80:669–695. [PubMed: 4773026]
32. Casjens, S.; Weigele, P. Viral Genome Packaging Machines: Genetics, Structure, and Mechanism. Springer; 2005. p. 80-88.
33. Johnson JE. Curr Opin Struct Biol. 2010; 20:210–216. [PubMed: 20149636]
34. Galisteo ML, King J. Biophys J. 1993; 65:227–235. [PubMed: 8369433]
35. Carrasco C, Douas M, Miranda R, Castellanos M, Serena PA, Carrascosa JL, Mateu MG, Marques MI, De Pablo PJ. Proc Natl Acad Sci U S A. 2009; 106:5475–5480. [PubMed: 19307554]
36. Hernando-Perez M, Cartagena-Rivera AX, Bozic AL, Carrillo PJP, Martin CS, Mateu MG, Raman A, Podgornik R, De Pablo PJ. Nanoscale. 2015; 7:17289–17298. [PubMed: 26228582]
37. Llauro A, Coppari E, Imperatori F, Bizzarri AR, Caston JR, Santi L, Cannistraro S, De Pablo PJ. Biophys J. 2015; 109:390–397. [PubMed: 26200875]
38. Hernando-Pérez M, Lambert S, Nakatani-Webster E, Catalano CE, De Pablo PJ. Nat Commun. 2014; 5:4520. [PubMed: 25072871]
39. Mateu MG. Virus Res. 2012; 168:1–22. [PubMed: 22705418]
40. Roos WH, Bruinsma R, Wuite GJL. Nat Phys. 2010; 6:733–743.
41. Rösler, J.; Harders, H.; Bäker, M. Mechanical behaviour of engineering materials:metals, ceramics, polymers, and composites. Springer; Berlin, New York: 2007.
42. Carrasco C, Carreira A, Schaap IAT, Serena PA, Gomez-Herrero J, Mateu MG, Pablo PJ. Proc Natl Acad Sci U S A. 2006; 103:13706–13711. [PubMed: 16945903]
43. Klug WS, Bruinsma RF, Michel JP, Knobler CM, Ivanovska IL, Schmidt CF, Wuite GJL. Phys Rev Lett. 2006; 97:228101. [PubMed: 17155845]
44. Roos WH, Gibbons MM, Arkhipov A, Uetrecht C, Watts NR, Wingfield PT, Steven AC, Heck AJR, Schulten K, Klug WS, Wuite GJL. Biophys J. 2010; 99:1175–1181. [PubMed: 20713001]
45. Llauro A, Guerra P, Irigoyen N, Rodriguez JF, Verdaguer N, De Pablo PJ. Biophys J. 2014; 106:687–695. [PubMed: 24507609]
46. Sun YH, Parker MH, Weigele P, Casjens S, Prevelige PE, Krishna NR. J Mol Biol. 2000; 297:1195–1202. [PubMed: 10764583]
47. Vella D, Ajdari A, Vaziri A, Boudaoud A. J R Soc, Interface. 2012; 9:448–455. [PubMed: 21831894]
48. Carnahan NF, Starling KE. J Chem Phys. 1969; 51:635–636.
49. Wu J, Prausnitz JM. Fluid Phase Equilib. 1999; 155:139–154.

50. Kado Y, Inoue T, Ishikawa K. Acta Crystallogr, Sect F: Struct Biol Cryst Commun. 2011; 67:1473–1479.
51. Yang F, Moss LG, Phillips GN. J Biolumin Chemilumin. 1997:375–382.
52. Hill, TL. An introduction to statistical thermodynamics. Courier Corporation; 2012.
53. Cordova A, Deserno M, Gelbart WM, Ben-Shaul A. Biophys J. 2003; 85:70–74. [PubMed: 12829465]
54. Snijder J, Uetrecht C, Rose RJ, Sanchez-Eugenia R, Marti GA, Agirre J, Guerin DMA, Wuite GJL, Heck AJR, Roos WH. Nat Chem. 2013; 5:502–509. [PubMed: 23695632]
55. Smith DE, Tans SJ, Smith SB, Grimes S, Anderson DL, Bustamante C. Nature. 2001; 413:748–752. [PubMed: 11607035]
56. Evilevitch A, Lavelle L, Knobler CM, Raspaud E, Gelbart WM. Proc Natl Acad Sci U S A. 2003; 100:9292–9295. [PubMed: 12881484]
57. Jin Y, Sdao SM, Dover JA, Porcek NB, Knobler CM, Gelbart WM, Parent KN. Virology. 2015; 485:128–134. [PubMed: 26245366]
58. Lander GC, Tang L, Casjens SR, Gilcrease EB, Prevelige P, Poliakov A, Potter CS, Carragher B, Johnson JE. Science. 2006; 312:1791–1795. [PubMed: 16709746]
59. Marabini R, Masegosa IM, San Martin MC, Marco S, Fernandez JJ, De la Fraga LG, Vaquerizo C, Carazo JM. J Struct Biol. 1996; 116:237–240. [PubMed: 8812978]
60. Pettersen EF, Goddard TD, Huang CC, Couch GS, Greenblatt DM, Meng EC, Ferrin TE. J Comput Chem. 2004; 25:1605–1612. [PubMed: 15264254]
61. Mindell JA, Grigorieff N. J Struct Biol. 2003; 142:334–347. [PubMed: 12781660]
62. Sorzano CO, Bilbao-Castro JR, Shkolnisky Y, Alcorlo M, Melero R, Caffarena-Fernandez G, Li M, Xu G, Marabini R, Carazo JM. J Struct Biol. 2010; 171:197–206. [PubMed: 20362059]
63. Scheres SH, Nunez-Ramirez R, Sorzano CO, Carazo JM, Marabini R. Nat Protoc. 2008; 3:977–990. [PubMed: 18536645]
64. Ludtke SJ, Baldwin PR, Chiu W. J Struct Biol. 1999; 128:82–97. [PubMed: 10600563]
65. Ortega-Esteban A, Horcas I, Hernando-Perez M, Ares P, Perez-Berna AJ, San Martin C, Carrascosa JL, De Pablo PJ, Gomez-Herrero J. Ultramicroscopy. 2012; 114:56–61. [PubMed: 22356789]
66. Sader JE, Chon JWM, Mulvaney P. Rev Sci Instrum. 1999; 70:3967–3969.
67. Horcas I, Fernandez R, Gomez-Rodriguez JM, Colchero J, Gomez-Herrero J, Baro AM. Rev Sci Instrum. 2007; 78:013705. [PubMed: 17503926]

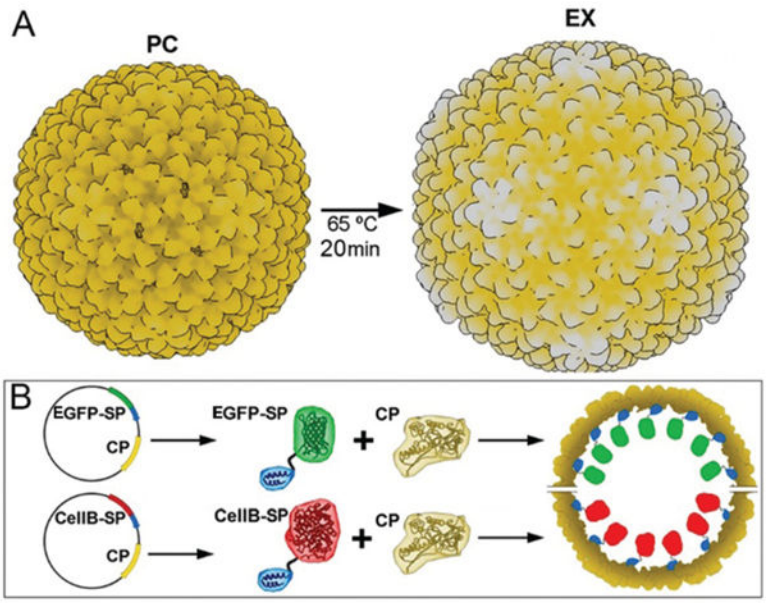

Fig. 1.

Synthesis of P22 nanocages and the expanded morphology of the P22 capsid. (A) P22 capsid maturation. P22 viral-like particles (VLP) are produced as procapsids (PC), which are transformed into an expanded shell form (EX) by heating at 65 °C for 20 min. (B) Assembly of P22 VLP with different cargos. Co-expression of coat protein (CP, yellow) with N-terminal truncated scaffold protein (SP, blue) fused to EGFP (green) or CelB monomers (red) leads to VLP assembly as PC with encapsulated cargo. VLP assembly is facilitated by an interaction of the essential SP C-terminal domain and CP subunits, which leads to encapsulation of SP-fused proteins. For clarity, EGFP and CelB are shown as monomers.

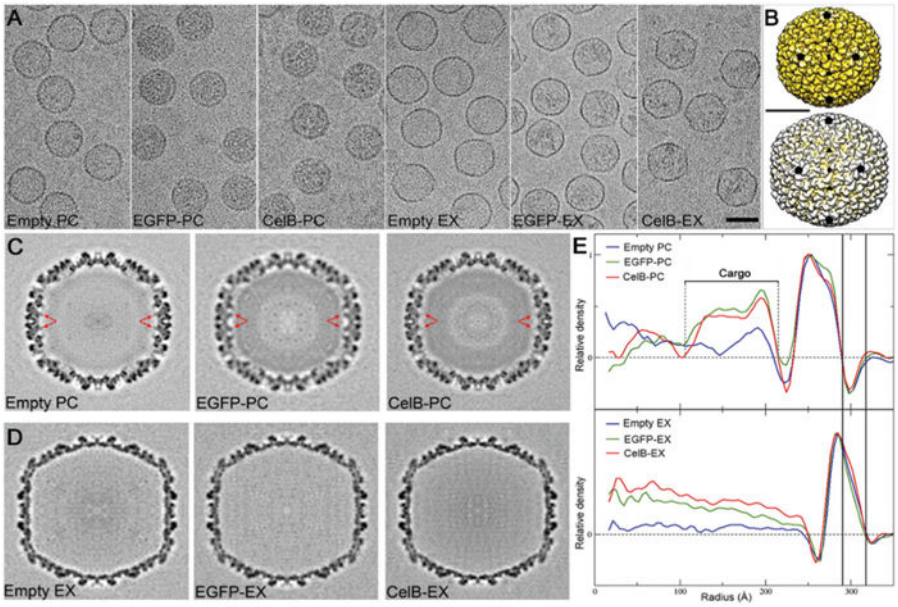

Fig. 2.

Three-dimensional cryo-EM reconstructions of empty, EGFP- and CelB-loaded P22 capsids. (A) Cryo-EM of (left to right) empty PC, EGFP-loaded PC (EGFP-PC), CelB-loaded PC (CelB-PC), empty EX, EGFP-loaded EX (EGFP-EX) and CelB-loaded EX (CelB-EX). Bar, 50 nm. (B) Surface-shaded representations of the outer surfaces, viewed along an icosahedral twofold axis, of P22 PC (top) and EX (bottom). Outer surfaces of empty and loaded PC and EX are similar at this resolution. Symbols indicate icosahedral symmetry axes. Bar, 25 nm. (C) Central sections from the 3DR viewed along a twofold axis of $T = 7$ empty PC (left), EGFP- (center) and CelB-PC (right). Darker shading indicates higher density. Arrows indicate some densities due to the SP C-terminal region in the PC internal surface (note that these densities are reduced in the CelB-PC central section). (D) Central sections from the 3DR viewed along a twofold axis of $T = 7$ empty EX (left), EGFP- (center) and CelB-EX (right). (E) Radial density profiles of 3DR of empty PC, EGFP- and CelB-PC, empty EX, and EGFP- and CelB-EX. PC (top) and EX shells (bottom) are essentially superimposable. In PC, a cargo shell spans radii from 107 to 216 Å. Vertical lines indicate PC (298 Å) and EX external radii (324 Å).

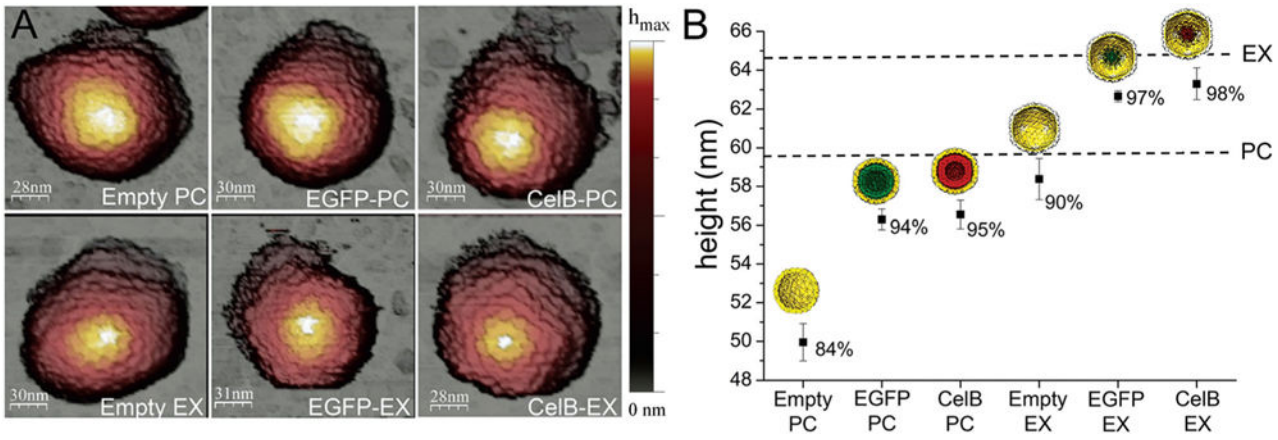

Fig. 3.

AFM topographies of P22 particles. (A) AFM images of empty PC, EGFP-PC, CelB-PC, empty EX, EGFP-EX and CelB-EX. Each image was normalized to its maximum height. (B) Heights of empty PC, EGFP-PC, CelB-PC, empty EX, EGFP-EX and CelB-EX after adsorption. Percentages indicate the ratio between average height as measured by AFM and nominal height based on 3D cryo-EM reconstructions. Dashed lines indicate nominal PC and EX outer diameters.

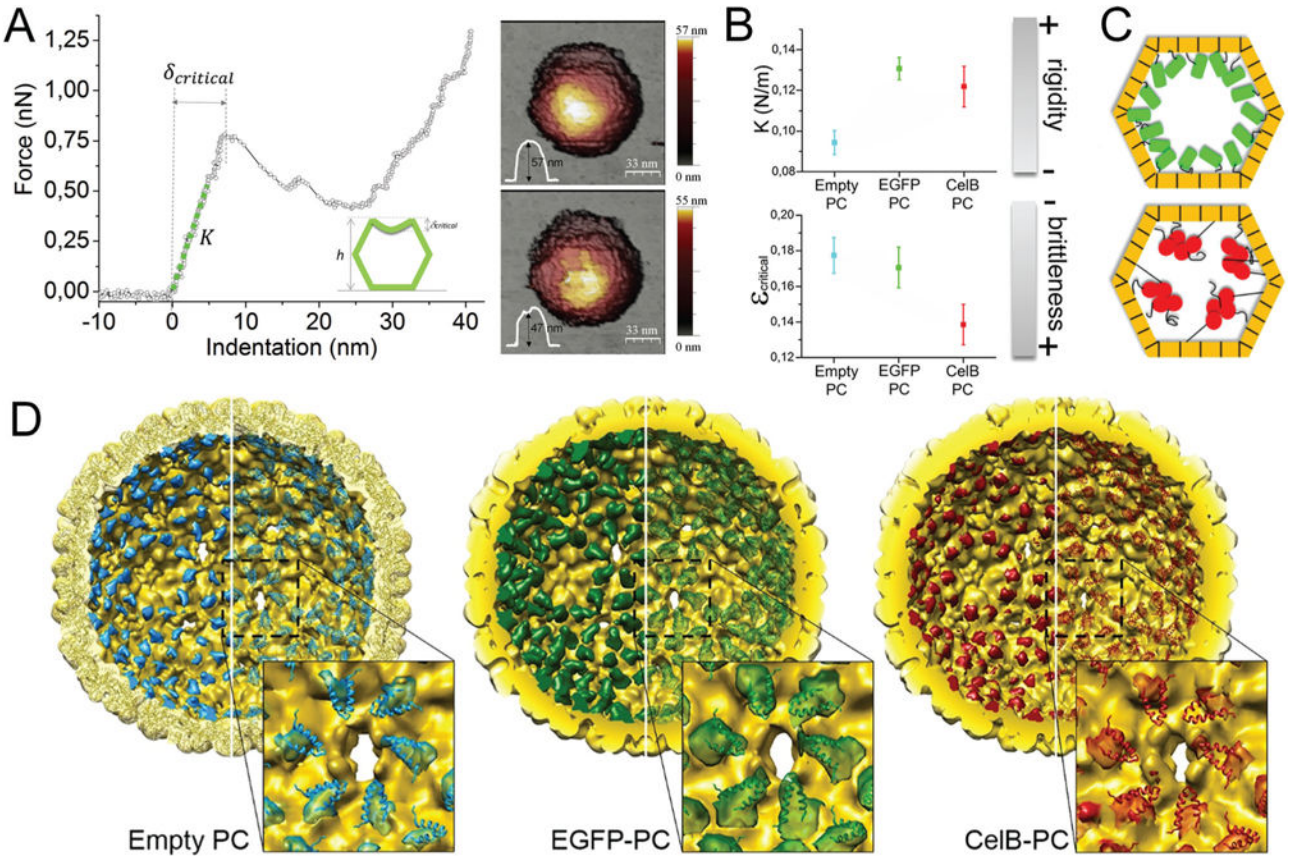

Fig. 4.

Structure and mechanical properties of P22 PC. (A) (Left) Typical force-vs.-indentation curve (FIC) of an EGFP-PC. Particle rigidity (k) and critical deformation (d_{critical}) can be calculated from the nanoindentation. Critical strain (e_{critical}), which provides information about particle deformation before breakage, is defined as the ratio between the critical indentation and particle height (inset). (Right) AFM topographies of the PC before (top) and after nanoindentation (bottom). A profile of the particle along its center is the inset in each image (bottom left). (B) Comparison of the average rigidity (top) and fragility (bottom) of empty and loaded PC. (C) Analysis of CP–SP interactions in empty and EGFP- and CelB-PC. PC viewed down a twofold axis from inside, with docked SP helix–loop–helix motif (right half). Empty PC shows the CP atomic model (yellow) in the shell and the SP motif in the SP density (blue; inset); the SP density is shown in EGFP-PC (green; center) and in CelB-PC (red; right). (D) Scheme of PC showing the organization of CelB tetramers (red, top) and EGFP monomers (green, bottom) fused to SP (black lines).

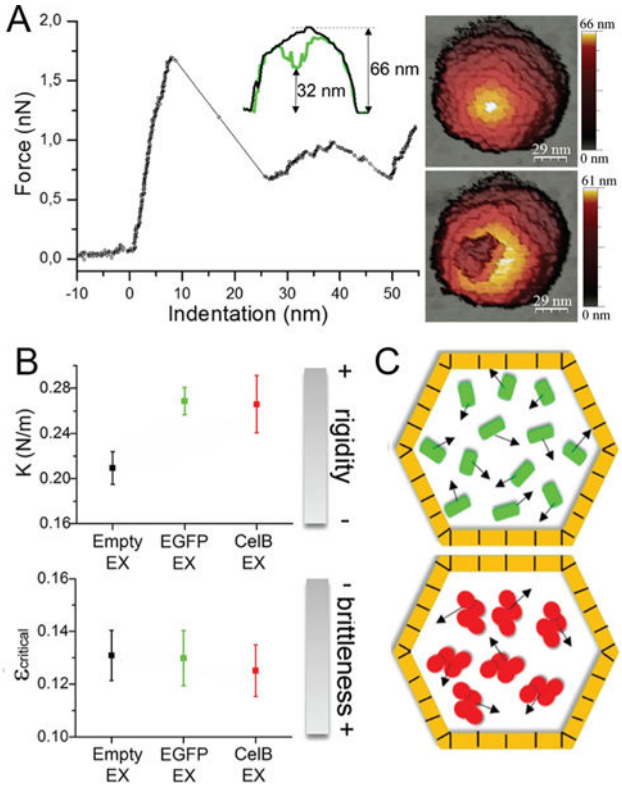

Fig. 5.

Mechanical characterization of EX capsids. (A) Typical FIC of a CelB-EX. Inset, aligned profiles of particle topographies before (black) and after (green) breakage. Right, CelB-EX images before (top) and after breakage (bottom). (B) Comparison of the average rigidity (top) and fragility (bottom) of empty and loaded EX. (C) Scheme of EX showing cargo units as diffusing entities within the protein shell (colors as in Fig. 4).

Table 1

Interactions that modulate P22 PC and EX mechanics. In PC, the cargo is constrained to the vicinity of the shell, whereas unattached cargo in EX moves freely inside the shell, creating osmotic pressure

	CelB-PC	EGFP-PC	CelB-EX	EGFP-EX
Physical origin	**Structural reinforcement**		**Steric interactions**	
Capsid volume (nm^3)	46 452		71 936	
#Cargo/capsid	32	224	32	224
Packing factor %	45	36	29	23
Pressure (MPa)	—	—	3 ± 1	3 ± 1